ADVANCING EARTH AND SPACE SCIENCES

JGR Planets

RESEARCH ARTICLE
10.1029/2024JE008679

Helium in Mercury's Extended Exosphere Determined by Pick-Up Generated Ion Cyclotron Waves

F. Weichbold[1], H. Lammer[1], D. Schmid[1], M. Volwerk[1], J. Hener[2], A. Varsani[1], A. Vorburger[2], P. Wurz[2], and C. Simon-Wedlund[1]

[1]Space Research Institute, Austrian Academy of Sciences, Graz, Austria, [2]Space Research and Planetology, Physics Institute, University of Bern, Bern, Switzerland

Key Points:

- First determination of He around Mercury based on magnetic field data
- Demonstration that He density measurements are consistent with a solar wind driven thermal He exosphere
- A non-thermal He population was found in measurement set, which could be caused by vapourization from sporadic meteorite impact events

Correspondence to:

F. Weichbold,
fabian.weichbold@oeaw.ac.at

Citation:

Weichbold, F., Lammer, H., Schmid, D., Volwerk, M., Hener, J., Varsani, A., et al. (2025). Helium in Mercury's extended exosphere determined by pick-up generated ion cyclotron waves. *Journal of Geophysical Research: Planets*, *130*, e2024JE008679. https://doi.org/10.1029/2024JE008679

Received 23 AUG 2024
Accepted 18 FEB 2025

Author Contributions:

Conceptualization: F. Weichbold, H. Lammer, D. Schmid
Data curation: F. Weichbold, J. Hener
Formal analysis: F. Weichbold, D. Schmid, J. Hener
Investigation: F. Weichbold, H. Lammer, D. Schmid, M. Volwerk
Methodology: F. Weichbold, H. Lammer, D. Schmid, M. Volwerk
Software: F. Weichbold, J. Hener, A. Vorburger
Supervision: H. Lammer, D. Schmid
Visualization: F. Weichbold
Writing – original draft: F. Weichbold, H. Lammer
Writing – review & editing: F. Weichbold, H. Lammer, D. Schmid, M. Volwerk, J. Hener, A. Varsani, A. Vorburger, P. Wurz, C. Simon-Wedlund

Abstract Helium (He) was first detected by remote spectroscopic observations of the Ultraviolet Visible Spectrometers (UVVS) instrument in Mercury's exosphere during the three Mariner 10 flybys in 1974 and 1975. Here, we derive the first in situ radial density profile of He in Mercury's extended exosphere by analyzing magnetic field and plasma measurements from 2011 to 2015 obtained by the MErcury Surface, Space ENvironment, Geophysics, and Ranging (MESSENGER) spacecraft. Our results indicate that most of the exospheric He follows a thermal trend. Interestingly, some events show density enhancements compared to the thermal profile which might be caused by sporadic (micro-)meteorite impact events. These energetic He population events yield average He surface densities of $\approx$150 cm^{-3}. The thermal He population on Mercury's day side can be reproduced with a surface density of $\approx$1,100 cm^{-3}. The main exospheric He source can be identified as thermal release and thermal recycling of solar wind implanted He particles that agree well with the observations made by the Probing Of Hermean Exosphere By Ultraviolet Spectrometer (PHEBUS) instrument on board BepiColombo during its first Mercury fly by and exospheric simulations.

Plain Language Summary Mariner 10 first identified the presence of a Helium (He) exosphere around Mercury through remote spectrometric observations during its flybys in 1974–1975. These observations were recently confirmed by the PHEBUS instrument onboard the BepiColombo spacecraft, which also detected exospheric He, albeit with a lower number density than that reported by Mariner 10. In this study, we present the first in situ density profile of He, derived from magnetic field and plasma measurements taken by the MErcury Surface, Space ENvironment, Geochemistry, and Ranging (MESSENGER) spacecraft. These data were analyzed to identify ion cyclotron waves (ICWs) generated by exospheric He^+ pick-up ions. Our findings indicate the existence of two distinct Helium populations around Mercury: one thermally released from the surface and another, more energetic and sporadic population likely caused by meteorite impacts that vapourize material on Mercury's surface. Based on our ICW analysis, the Helium abundance in Mercury's extended exosphere is expected to vary depending on the parameters of impacting (micro-)meteorites, such as their frequency and intensity.

1. Introduction

In 1974, the Mariner 10 spacecraft provided the first evidence that Mercury, the innermost planet of our Solar System, possesses a thin, collisionless gaseous envelope representing an exosphere where the exobase level corresponds to the surface. Further analysis of the Mariner 10 data unveiled the presence of various gaseous constituents within this exosphere, originating from sources such as the planetary surface, the solar wind, and even (micro-) meteorites. Notably, Mariner 10's UV spectrograph detected for the first time an abundance of Helium (He) at the 58.4 nm resonance line (Broadfoot et al., 1974, 1976; Hartle et al., 1975). The radiance of photons emitted at the wavelength of the resonance line along a line-of-sight (LOS) was measured. Based on the measured radiance's the column density of the photon-emitting He content within this LOS could be estimated. Collecting radiance measurements from multiple LOSs makes it possible to construct a density profile of He (Broadfoot et al., 1974). After analyzing the Mariner 10 data the determined He surface number density was estimated to be $\sim$4,500 cm^{-3} to 6,000 cm^{-3} based on the observations of the 1st and 3rd Mercury encounter (Broadfoot et al., 1976; Hunten et al., 1989).

Nearly four decades later, the MESSENGER spacecraft confirmed the presence of planetary Helium ions, He^+, at different radial distances to the planet by measurements of the energy, angular, and compositional profiles of the low-energy components of the ion distributions with the Fast Imaging Plasma Spectrometer (FIPS) (Andrews et al., 2007; Raines et al., 2013). Using the FIPS instrument Raines et al. (2013) determined a He^+ density profile depending on the local time. A more recent study conducted by Wurz et al. (2019) reproduced the FIPS He^+ data by using the modeled He neutral density profile of Wurz and Lammer (2003), which is based on the thermal release of He from Mercury's surface with a surface number density in agreement with the estimates from the Mariner 10 data. Previous studies show that the solar wind is the main contributor to Mercury's exospheric He content (Goldstein et al., 1981; Grava et al., 2016; Hartle et al., 1975; Hunten et al., 1989; Hurley et al., 2016). The He ions from the solar wind can reach the planet's surface by penetrating directly through the cusp regions when the interplanetary magnetic field (IMF) is in a favorable orientation (Goldstein et al., 1981; Kallio & Janhunen, 2003; Killen et al., 2001). Surface particles are released into Mercury's exosphere through various particle release mechanisms (Wurz et al., 2022). Thermal release is the primary mechanism governing the content of very light and volatile materials such as solar wind-implanted He (Killen et al., 2007; Wurz et al., 2022; Wurz & Lammer, 2003).

Schmid et al. (2022) analyzed for the first time H^+ Ion Cyclotron Waves (ICWs) in the magnetic field data of the MESSENGER spacecraft, which were specifically generated by freshly ionized pick-up ions and determined the local number density of neutral hydrogen atoms. Here we apply the method presented by Schmid et al. (2022) to study He in Mercury's exosphere.

Section 2 describes the method that is used to identify ICWs generated specifically by the pick-up of freshly ionized planetary He atoms in Mercury's extended exosphere. Utilizing the observed wave power of these identified ICWs, we deduce the local exospheric He neutral density that was necessary for producing the He^+ pick-up ions during the detection period. This enables us to reconstruct an in situ altitude-dependent density profile of He atoms around Mercury from the surface up to distances of several Mercury radii. In Section 3 and 4 we discuss the observation results, characterize our findings, and compare them with previous UVVS observations of Mariner 10 and BepiColombo.

2. Materials and Methods

2.1. ICW Generation Mechanism

Ion cyclotron waves (ICWs) are generated in a plasma by a temperature anisotropy, where the temperature perpendicular to the background magnetic field is higher than the parallel temperature (Gary, 1991). Solar photons ionize exospheric particles like He, producing free electrons and He^+, which are subsequently picked-up by the solar wind and begin to gyrate around the local magnetic field. Due to the difference in velocity between the newly created ions, which are initially at rest relative to Mercury, and the IMF, moving at the solar wind speed, this pick-up process forms a ring-beam distribution in velocity space, which is unstable for different plasma instabilities. Depending on the plasma-β this can either produce mirror modes (zero-frequency "waves" characterized by magnetic and plasma density variations in anti-phase, see (S. P. Gary et al., 1993; Hasegawa, 1969; Southwood & Kivelson, 1993)) for high-β, or produce ICWs (transverse waves) for low-β plasmas. Here "high" and "low" is relative, as for both instabilities $\beta > 1$. Waves created by ion pick-up around a planet or moon are characterized, in the spacecraft frame, by their frequency and polarization. An ion of mass m_i and charge q_i in a background magnetic field strength B_0 will have a gyro frequency of $\Omega_i = q_i B_0 / m_i$. The magnetic field $\vec{B}$ is assumed to pass by the celestial object with a certain velocity $\vec{v}$, and will, most likely, not be perpendicular to the velocity. This means that pick-up ions will have a drift velocity $\vec{v}_{\|}$ along the field. A resonance with the ambient wave-spectrum in the plasma can occur with waves of frequency ω and wave vector $\vec{k}$, with a frequency of $\omega' = \omega - \vec{k} \cdot \vec{v}_{\|}$ in the pick-up particle's frame (Brinca, 1991), when

$$\omega - \vec{k} \cdot \vec{v}_{\|} = \pm \Omega_i. \tag{1}$$

Resonance will mainly occur with the right-handed mode in the plasma frame, described by the − sign. Assuming that the velocities of the spacecraft and the ionizing neutrals are negligible with respect to the pick-up velocity, then in the spacecraft frame the waves will be observed Doppler-shifted as:

$$\omega_{SC} = \omega + \vec{k} \cdot \vec{v}_{\|}, \tag{2}$$

which finally results in observations at:

$$\omega_{SC} \approx \Omega_i, \tag{3}$$

with left-hand polarization. This specific process is known as the anomalous Doppler effect, see Mazelle and Neubauer (1993) and Delva et al. (2008). Numerical studies have shown that the observed wave power is usually at a frequency slightly below the local gyro frequency, with the amount depending on the composition of the background plasma (Rönnmark, 1982). Spectral analysis of magnetometer data can show evidence of the presence of multiple pick-up ions (Volwerk et al., 2001, 2010), however, considering that ICWs do not distinguish between ions with the same mass-to-charge ratio. Pick-up ICWs have been observed at various locations in the solar system: at Venus (Delva et al., 2008, 2009, 2011, 2015); at Mercury (Schmid et al., 2021, 2022); at Mars (Brain et al., 2002; C. T. Russell et al., 1990) and at Jupiter's Galilean satellites (Huddleston et al., 1998; C. Russell et al., 1998; Volwerk et al., 2001). Data from the magnetometer onboard Galileo showed the presence of SO_2 and SO coming from Io and a slew of sputtered ions around Europa (e.g., Na, O_2 and both positively and negatively charged Cl, C. Russell (2005)). In the context of cometary plasma physics, Huddleston and Johnstone (1992) discussed how the pick-up ions at comet Halley represent a "free energy" that can be converted into wave energy through scattering of the ring-distribution ions into a bi-spherical shell distribution. The free energy can be expressed as:

$$E_{\text{free}} = \frac{1}{4}\Phi m_i N_{\text{pu}} V_{\text{A}} V_{\text{inj}}\left[(1+\cos(\alpha))^2 + (1-\cos(\alpha))^2\right], \tag{4}$$

where $\alpha = \angle(\mathbf{v}_{\text{inj}}, \mathbf{B})$. Assuming complete scattering of the ring distribution, $\Phi = 1$, the energy in the waves should be equal to the free energy. In order to obtain the energy in the waves, the peaks in the power spectra of the magnetometer data are integrated over an appropriate frequency range around the gyro frequency (Delva et al., 2008). This energy, E_{wave}, can then be equated to the free energy of the ring distribution E_{free}. However, numerical simulations have shown that the efficiency of converting particle to wave power is around $\Phi \approx 0.3$ (Cowee et al., 2007). Equation 4, with $\Phi = 1$ and $E_{\text{free}} = E_{\text{wave}}$, can be inverted to obtain a lower limit for the pick-up density N_{pu}. With a model for the neutral "outgassing" of Io and an ionization rate of the neutrals, a source rate for the neutral gas can then be determined.

2.2. Identification and Criteria of ICWs Generated by He^+ Pick-Up Ions

The methodology employed within this study to identify He^+ pick-up generated ICWs is derived from the concept developed by Huddleston et al. (1991) and later by Delva et al. (2008, 2009). This approach was applied and further developed by Schmid et al. (2022) for the analysis of Mercury's hydrogen exosphere. For the study of ICWs generated by He^+, a wave analysis of the 20 Hz magnetic field data, which were obtained from the MESSENGER spacecraft (Anderson et al., 2007; Solomon et al., 2007) during its mission from March 2011 to April 2015, were used. A sliding window with a length of ≈ 100 s is applied to the data over which the field is averaged to obtain a background field from which the Mean Field Aligned (MFA) coordinate system is produced. The parallel component is defined as:

$$\hat{e}_{\parallel} = \frac{\mathbf{B_0}}{|\mathbf{B_0}|}, \tag{5}$$

along to the mean magnetic field. The other two axes $\hat{e}_{\perp 1}$ and $\hat{e}_{\perp 2}$ are perpendicular to $\hat{e}_{\parallel}$ and defined as:

$$\hat{e}_{\perp 1} = \hat{e}_{\parallel} \times e_z \tag{6}$$

$$\hat{e}_{\perp 2} = \hat{e}_{\perp 1} \times \hat{e}_{\parallel} \tag{7}$$

where $e_z = [0, 0, 1]$ is the unit vector along the z-axis in the MSO-frame.

Based on the method by Welch (1967), the sliding window interval is divided into three sub-intervals with an overlap of 50%. By Fourier transforming the data, the power spectral density (PSD) matrix can be obtained for each sub-interval. The diagonal elements of the PSD-Matrix give the power densities in the corresponding directions ($P_{\parallel}$; $P_{\perp} = \frac{1}{2}(P_{\perp 1} + P_{\perp 2})$). Out of the off-diagonal elements of the PSD-Matrix the handedness, the ellipticity ϵ, and the wave propagation vector $\mathbf{k}$ of the wave can be obtained (Means, 1972; Narita, 2017; Samson & Olson, 1980).

Since the velocity of the planetary ions is negligible in comparison with the velocity of the spacecraft, the generated ICWs are observed around the local ion gyro-frequency (Delva et al., 2008):

$$f_{\text{gyro}} = \frac{qB_0}{2\pi m_i} \tag{8}$$

where m_i represents the ion mass, q is the charge, and B_0 is the average magnetic field (Delva et al., 2008; Huddleston, 1990). Additionally, an error range for the ion gyro-frequency, Δf_{gyro}, is computed as:

$$\Delta f_{\text{gyro}} = \frac{q\sigma_B}{2\pi m_i}, \tag{9}$$

where σ_B denotes the standard deviation of the magnetic field within the 100 s interval. To reliably identify the ICWs, the arithmetic means of the power densities and the ellipticity of the wave, and the median of the wave-propagation vector within the sliding window are computed and checked if they match the following criteria within the frequency range $\Delta F = \left[0.8 \cdot (f_{\text{gyro}} - \Delta f_{\text{gyro}}); f_{gyro} + \Delta f_{\text{gyro}}\right]$:

- The power densities ($P_{\parallel}$ and $P_{\perp}$) are integrated over the frequency range ΔF. To assure that the obtained wave is mainly transverse the integrated power in the perpendicular component $\left(E_{\perp} = \int_{df} P_{\perp} df\right)$ must exceed the power of the parallel component $\left(E_{\parallel} = \int_{df} P_{\parallel} df\right)$ by a factor of 5.
- To assure that the obtained wave is left-handed and circular polarized the ellipticity $\epsilon < -0.55$.
- To confirm that the wave propagates along the mean magnetic field, the wave vector $\mathbf{k}$ is calculated for each frequency within the frequency range ΔF and the angle ϕ between $\mathbf{k}$ and $\mathbf{B_0}$ in the frequency range is computed. Since ICWs propagate quasi-parallel to the magnetic field we require $\phi < 35°$.

Additionally, the solar zenith angle (SZA) is determined for each ICW event, ensuring that the ICW observations occur on the dayside of the planet (SZA <90°). Furthermore, only events located outside the bow shock of Mercury are considered for this study. To determine this, the boundary data set from Philpott et al. (2020) is employed. These two criteria are applied to the selected events to ensure that the ICWs are freshly generated and to exclude waves that may be diminishing, meaning waves that have propagated and begun to lose energy or amplitude as they travel away from their source, as discussed by Delva et al. (2009).

In Figure 1 an example of an identified ICW is shown in the MFA-coordinate system. The fluctuations transverse to the background magnetic field direction (yellow and red) dominate over the fluctuations along the magnetic field direction (blue), which indicates an in-compressible wave. This behavior can also be seen in Figure 2 because the power of the perpendicular component (red) is larger then that in the parallel component (blue) by a factor of ~10, also indicating a mainly transverse wave that peaks at local gyro-frequency of He (marked with the black solid line). The gray box between the two dashed lines indicates the integration frequency range ΔF in which the wave properties are evaluated.

2.3. Determination of the Exospheric He Density

To estimate the He particle density in the exosphere of Mercury, we first determine the density of the He^+ pick-up ions, necessary to excite the observed waves (Delva et al., 2009; Huddleston & Johnstone, 1992; Schmid et al., 2022; Volwerk et al., 2010). The pick-up ion density n_{ion} can be calculated with (Huddleston et al., 1991):

$$n_{\text{ion}} = \frac{4E_{\text{free}}}{m_{\text{i}}\, v_{\text{inj}}\, v_{\text{A}}\left[(1+\cos(\alpha))^2 + (1-\cos(\alpha))^2\right]}, \tag{10}$$

where m_{i} is the ion mass, $\vec{v}_{\text{inj}}$ is the injection velocity, the angle between v_{inj} and the mean magnetic field $\mathbf{B_0}$ is denoted as α, E_{free} represents the free energy and v_{A} is the local Alfvén velocity, $v_{\text{A}} = \mathbf{B_0}/\sqrt{n_{\text{SW}}\, m_{\text{p}}\, \mu_0}$, where μ_0 is the permeability of free space, n_{sw} represents the density of the solar wind and m_{p} is the mass of a proton,

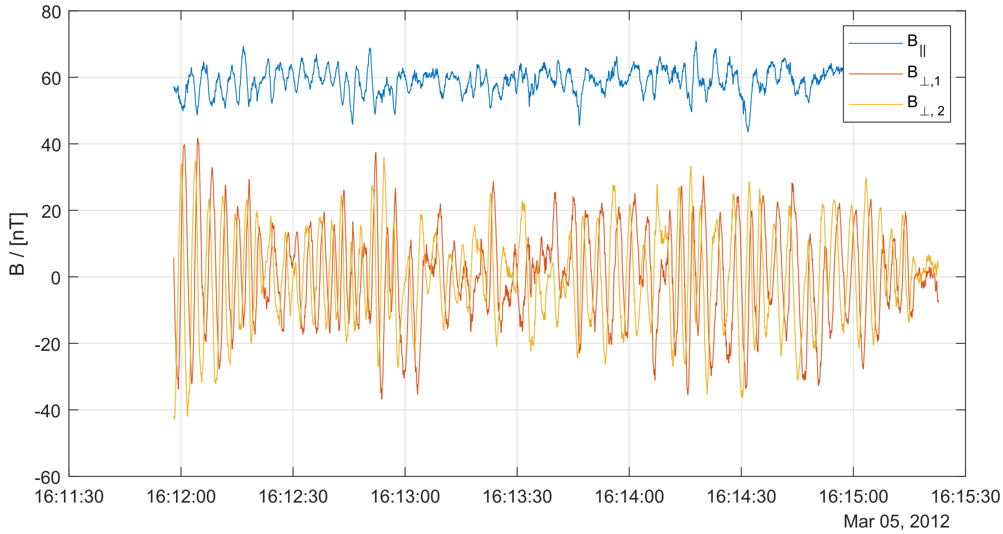

Figure 1. The magnetic field observations in Mean-Field-Aligned coordinates of an identified ICW-event generated by He^+ pick-up ions. Here $B_{\|}$ is in the direction parallel to the mean magnetic field within the sliding window. $B_{\perp 1}$ and $B_{\perp 2}$ are perpendicular to each other and the $B_{\|}$ direction.

assuming that the solar wind is composed only of protons. The total free energy $\left(E_{\text{free}}\right)$ is the energy that is available to excite a cyclotron wave from the pick-up ion ring-beam distribution (Huddleston, 1990; Huddleston & Johnstone, 1992), and can be derived from the observed wave power and following relation (Delva et al., 2009; Schmid et al., 2022):

$$E_{\text{free}} = \eta \frac{1}{2\mu_0} \int_{\Delta F} P_{\perp} df. \tag{11}$$

here η is the so-called efficiency parameter that describes how much energy from the particles in the ring distribution is transferred to the wave. Previous studies have assumed that the entire energy from the particle is used to excite the wave, that is, $\eta = 1$ (Delva et al., 2009; Huddleston & Johnstone, 1992; Schmid et al., 2022).

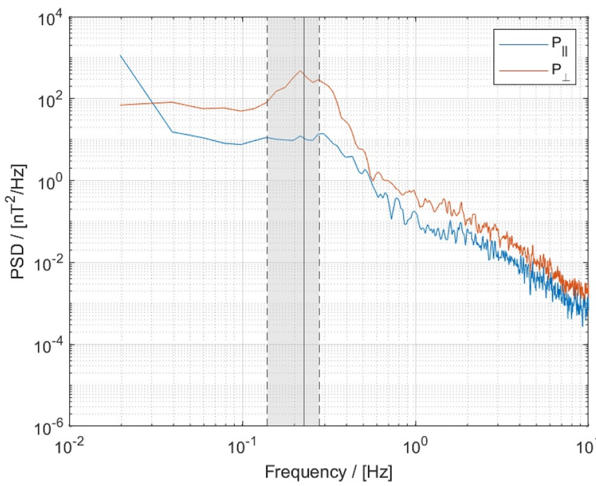

Figure 2. Power Spectrum of the identified event shown in Figure 1. The blue line represents the power density in the component parallel to the magnetic field $\left(P_{\|}\right)$, while the orange line indicates the Power density in the perpendicular component $\left(P_{\perp}\right)$. The gray box indicates the integration frequency range.

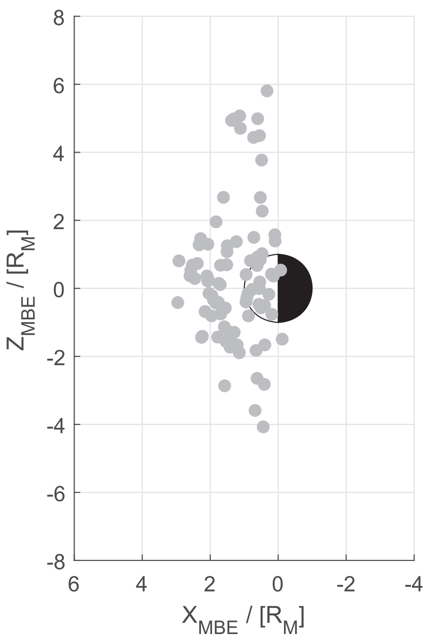

Figure 3. Observational evidence that the ion cyclotron waves are generated locally by freshly ionized ions.

However, simulations showed that $\eta = \frac{1}{3}$ is more realistic (Cowee et al., 2012), because the energy from ions is distributed between wave growth and ion heating. Within our analysis we thus the latter value of $\eta = \frac{1}{3}$.

Since the new born planetary ions have a negligible velocity compared to the solar wind, the injection velocity v_{inj} corresponds to the solar wind velocity. However, due to the nadir-pointing configuration of the MESSENGER spacecraft, the plasma instrument is potentially shielded by the Sun shield causing a limited field of view (FOV), which means that the MESSENGER plasma observations are limited to determine v_{inj}. To overcome this problem, the solar wind propagation model from Tao et al. (2005) is utilized. This model provides estimations for the solar wind velocity $\vec{v}_{\text{sw}}$ and plasma density n_{sw} during the ICW observations at Mercury. The injection velocity $\vec{v}_{\text{inj}}$ is calculated by $\vec{v}_{\text{inj}} = -\vec{v}_{\text{sw}} + \vec{v}_{\text{mer}}$, where $\vec{v}_{\text{mer}}$ represents the orbital velocity to account the aberration of the solar wind, due to the orbital motion of Mercury around the Sun (Acton, 1996).

Following Schmid et al. (2022), the neutral gas density n can then be estimated by

$$n = \frac{2\pi f_{\text{gyro}}\, n_{\text{ion}}}{100\, \nu}, \tag{12}$$

where f_{gyro} is the local gyro-frequency of the pick-up ion and n_{ion} is the obtained ion density from Equation 10. Based on simulation results we employ a characteristic time ($\Omega_{\text{He}}\, t$) equivalent to 100 gyro-periods until the ICWs reach their full development and attain a quasi-steady state. The choice of 100 gyro-periods, although conservative, is based on computer simulations indicating that complete energy transfer from ions to waves occurs over approximately 60–100 ion gyrations (Cowee et al., 2012). Finally, ν, the ionization rate of helium (He) into He^+, is influenced by two main processes: photo-ionization and charge exchange between fast solar wind protons and background He atoms. Photo-ionization, on the other hand, depends on both solar activity and Mercury's orbital distance from the Sun. The ionization rate for this process is derived from Huebner and Mukherjee (2015) and adjusted using the Flare Irradiance Spectral Model-Planetary (FISM-P; Chamberlin et al. (2008)). FISM-P extrapolates the solar irradiance at Earth to the orbits of planets within the solar system. To standardize the solar irradiance, a normalized index is used, where 0 corresponds to the minimum solar irradiance and 1 corresponds to the maximum flux at 58.4 nm during solar cycle 24, as observed during the MESSENGER mission. Using this normalized irradiance, the photo-ionization rate is determined to range from $2.63 \times 10^{-7}\ \text{s}^{-1}$ to $1.66 \times 10^{-6}\ \text{s}^{-1}$. On the other hand, charge exchange plays only a minor role in the ionization of He^+ near Mercury. To support this, we note that the typical solar wind proton number flux near Mercury is approximately $1 \times 10^9\ \text{cm}^{-2}\ \text{s}^{-1}$ at 400 km/s (Sun et al., 2021). The cross-section for $\text{He}^+ + \text{He}$ charge exchange is less than $1 \times 10^{-18}\ \text{cm}^2$ around 1 keV proton energy (Gruntman, 1997), resulting in an ionization rate of only $1 \times 10^{-9}\ \text{s}^{-1}$. This rate is orders of magnitude lower than the photo-ionization rate and is therefore negligible. As a result, only photo-ionization is considered for the calculation of the neutral gas density.

To confirm that the determined ICW events are freshly generated the observations are transferred into the so-called MBE-coordinate system (Mercury-Magnetic-Electric coordinate system). In this coordinate system the $\vec{x}_{\text{MBE}}$ axis points toward the Sun, in the direction of the injection velocity $\vec{V}_{\text{inj}}$. This means that it aligns with the solar wind flow. The $\vec{y}_{\text{MBE}}$ axis is positive in the direction of the component of the mean magnetic field B_0. Lastly, the $\vec{z}_{\text{MBE}}$ axis is positive in the direction of the convection electric field $\vec{E}$, which is given by the vector cross product of $\vec{V}_{\text{inj}}$ and B_0. In Figure 3 the identified events are uniformly distributed around $\pm\vec{z}_{\text{MBE}}$. Because there is no known mechanism to transport ions across the magnetic field against the electric field and into the negative electric field region, the generation of ICWs needs to occur locally (Delva et al., 2011). Hence, we infer that the observed ICWs are indeed locally generated, satisfying the underlying assumptions necessary for an on-site

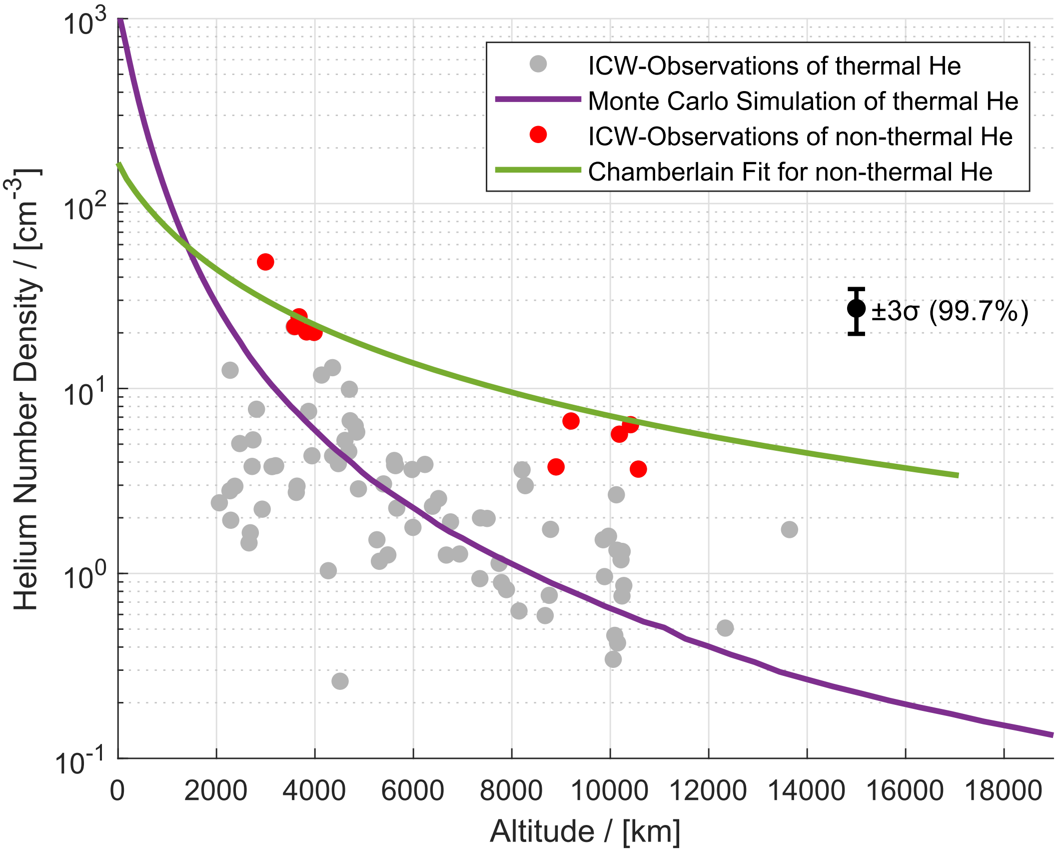

Figure 4. Altitude dependent density profile of neutral He in Mercury's exosphere. The dots indicate the He ion cyclotron wave observations. The violet line shows the result from a Monte Carlo simulation for thermal He. Therefore, all gray dots represent He-observation released in thermal processes, while the red dots show non-thermal He-observations. A least square fit of the red dots yielded the green Chamberlain profile.

density estimation. Another indication that the ICWs were freshly generated is that all events have a positive $\vec{x}_{\mathrm{MBE}}$ coordinate.

3. He Density Profile and Sources

So far only remote spectroscopic observations from Mariner 10 and BepiColombo as well as exospheric simulations were used to determine the neutral gas density of He around Mercury. In Figure 4 the first number density profile of He in Mercury's extended exosphere derived from in situ magnetic field measurements. Within this study, 85 He-ICWs were identified, and based on Equation 10 and Equation 12 the neutral gas density of each event was estimated.

In the next step, possible sources of the observed He are investigated. A previous study by Goldstein et al. (1981) investigated the possible surface interaction mechanisms and release processes of He into Mercury's exosphere. After He ions are implanted in several atomic depths into Mercury's surface He can leave the surface via (a) thermal diffusion, (b) surface sputtering, (c) sputter-diffusion, (d) erosion caused by (micro-) meteoroid impact vapourization (MIV), and (e) chemical reactions in the surface layers that are followed by one of the above-mentioned mechanisms. While all of these processes may be acting, Goldstein et al. (1981) conclude that diffusion-related processes are likely the most relevant for the release of the highly volatile Helium. Since the characteristic lifetime of Helium in Mercury's exosphere is long (<10 days or longer, e.g., Hener et al., 2024; Quémerais et al., 2023) and at any time the vast majority of the exospheric content has been "recycled" after returning to the surface, it is in any case not the release process, but the mechanics of the surface recycling interaction, which drives the characteristics of the exosphere (Hartle et al., 1975; Leblanc & Chaufray, 2011).

To evaluate the contribution of thermal helium density in Mercury's exosphere, we used an ab-initio semi-analytical model based on the assumption that the surface regolith is saturated with helium. This model assumes a steady-sate, solar wind-driven helium exosphere and follows the specific distribution law from Hodges and Johnson (1968) (i.e., $n \times T_{\mathrm{surf}}^{5/2} = \mathrm{const}$), without relying on ICW measurements. Furthermore, we assume a solar wind implantation at an average rate of $2.5 \times 10^{23}\ \mathrm{s}^{-1}$ and determine the global loss fraction for both escaping and ionized particles (Winslow et al., 2012). This fully defines the flux distribution over Mercury's surface. Using a 1D Monte Carlo simulation (Wurz & Lammer, 2003), we can compute the local radial exospheric density profiles according to the parameters defined by our surface distribution model. A more detailed description of this model is given in Hener et al. (2024). The model yields a representative dayside radial profile with a surface temperature of $T_{\mathrm{surf}} = 615\ \mathrm{K}$ and a surface number density of $n_{\mathrm{surf}} = 1{,}100\ \mathrm{cm}^{-3}$ (see purple profile in Figure 4). This profile aligns well with prior observations of thermal He around the planet: Quémerais et al. (2023) derived $n_{\mathrm{surf}} = 600\ \mathrm{cm}^{-3}$ to $1{,}000\ \mathrm{cm}^{-3}$ with a derived $T_{\mathrm{surf}} = 450\ \mathrm{K}$ to $550\ \mathrm{K}$ from measurements of the BepiColombo PHEBUS instrument over the terminator region and Mariner 10 UVS measurements lead to the somewhat larger dayside density n_{surf} values between $1{,}500\ \mathrm{cm}^{-3}$ (Hartle et al., 1975), $4{,}500\ \mathrm{cm}^{-3}$ (Broadfoot et al., 1976) and $6{,}000\ \mathrm{cm}^{-3}$ (Hunten et al., 1989) with a considered surface temperature of 575 K (Broadfoot et al., 1976).

The thermal steady-state model curve is given with a confidence interval of factor ±2 (Hener et al., 2024). Certainly, short-term variations in the solar wind implantation rates or heightened photo-ionization rates, both of which can be a function of solar activity and extreme events, can temporarily amplify He release and loss rates beyond factor ±2. Taking into account, however, the characteristic scale time of Mercury's He exosphere, which is quoted as 10 days (Quémerais et al., 2023) or some tens of days (Hener et al., 2024), these extreme events will have to be sustained on comparable time scales, which is typically not the case for for example, coronal mass ejections (Thatcher & Müller, 2011). Additionally, a Monte Carlo error propagation through the measurement technique (Equations 10 and 12) gave 3-σ confidence bounds of ±25% on the abundance measurements.

The population of red dots within Figure 4 are incompatible with the model of the steady-state thermal exosphere and its confidence intervals, suggesting that this population might have its origin in a different release process. A possible source were Solar wind alpha particles (He^{2+}) that are backscattered from the planetary surface a as energetic neutral atoms (ENAs), which may become photo-ionized again. Nevertheless, it is unlikely that these ENAs are the source of the observed non-thermal helium ions. This is because the backscattered helium neutrals have velocity very different from the S/C frame of reference. Therefore, He ENAs originating from the solar wind, which are later ionized, will excite pick-up ICWs at frequencies significantly different from the local ion gyrofrequency due to a Doppler-shift (Mazelle & Neubauer, 1993). To further investigate its source, a Chamberlain-profile was fitted to the incompatible population in Figure 4, indicating a non-thermal helium release process with a best-fit temperature of $T_{\mathrm{surf}} = 2700\ \mathrm{K}$ and a surface number density of approximately $n_{\mathrm{surf}} = 150\ \mathrm{cm}^{-3} \pm 10\%$. This temperature aligns with ranges reported for particles released by meteorite impact evaporation (Berezhnoy & Klumov, 2008; Eichhorn, 1978).

While Mercury is exposed to a constant influx of micro-meteoroids (Cintala, 1992), which impact the surface and facilitate this non-thermal vapourization release, it is typically not a dominant source process for exospheric species (see e.g., Killen et al. (2007) and Morgan et al. (1988) for Na and Wurz et al. (2010) for Na, K, and O). This also applies to the helium exosphere: the fit to the non-thermal population in Figure 4 indicates a surface density of $150\ \mathrm{cm}^{-3} \pm 10\%$ He population, which, if to be part of the global steady-state of the system, requires a MIV surface erosion flux of $\approx 7.5 \times 10^{7}$ He $\mathrm{cm}^{-2}\ \mathrm{s}^{-1}$. Note that, besides being incompatible with the expected impactor flux at Mercury (Marchi et al., 2005), it is also two orders of magnitude greater than the primary He supply through the solar wind ($\approx 3.3 \times 10^{5}$ He $\mathrm{cm}^{-2}\ \mathrm{s}^{-1}$), which would result in a rapid depletion of He in the system. However, as demonstrated by Mangano et al. (2007), individual medium to large impactors can produce transient abundance enhancements of refractory species in the exosphere around the impact site. Hener et al. (2024) demonstrate that the same is true for helium: their simulations show that impactors between 0.5 m and 1 m in radius could produce significant helium enhancements over an angular range of $\pm 30^{\circ}$ to $\pm 60^{\circ}$ for several thousand seconds, suggesting that meteorite impacts are a possible origin of non-thermal helium measurements. A detailed analysis of meteorite sizes, impact yield and in situ detection probability of such events is presented in (Hener et al., 2024).

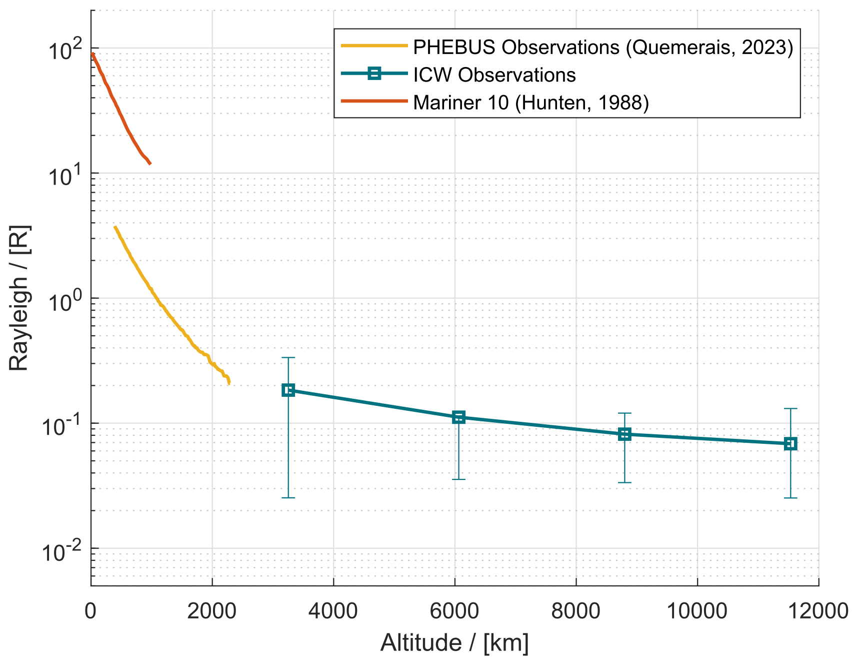

Figure 5. Airglow of He radiances in Mercury's exosphere.

4. Discussion

To compare the He particle densities obtained in Figure 4 with previous observations, we transform the He densities into radiances. To determine the brightness B of a spectral line based on the neutral gas density, the approach shown in Chamberlain and Hunten (1987), as well as Hunten et al. (1989) is followed and yields to

$$B = \frac{1}{4\pi\ 10^6}\, p(\theta)\ g\ N, \tag{13}$$

where $p(\theta)$ represents the scattering phase function, which is set to one in our analysis to assume isotropic scattering, g expresses the excitation factor and N is the column density along a line-of-sight (LOS). The integrated column density can be expressed as (Chamberlain & Hunten, 1987)

$$N = 2n(r)re^{\frac{r}{H}}K\left(\frac{r}{H}\right) \approx N(r)\sqrt{2\pi rH}\left(1 + \frac{3}{8}\frac{H}{r} + \ldots\right). \tag{14}$$

here, n represents the local density, H is the scale height, which is determined by e-folding of the determined density profile, at a specific r, which is the radial distance from the center of the planet and K is the modified Bessel function of third kind.

The yellow line in Figure 5 represents data collected by the PHEBUS instrument during the first Mercury fly by of BepiColombo (Quémerais et al., 2023). Notably, they recorded radiances of approximately 4 R at an altitude of roughly 470 km, which then declined to around 0.25 R as the altitude reached about 2000 km. Note that the ICW observations (blue line) were conducted at higher altitudes and so the radiance values derived from the determined He number density start at an altitude of approximately 3500 km with a value of roughly 0.1 R. To estimate the Rayleigh scattering around Mercury, boxplots were calculated in 1 R_M bins, with the median and the upper and lower quartiles taken as the representative values, which are then shown in Figure 5. Figure 5 clearly illustrates that the radiance values obtained from Quémerais et al. (2023) and the He number density derived in this study align very well.

Remarkably, radiance values of Quémerais et al. (2023) and this study are more than one order of magnitude lower than those given in (Broadfoot et al., 1974, 1976; Hunten et al., 1989). Consequently, a reevaluation of the values presented in Hunten et al. (1989) was conducted, resulting in the following findings. The g-value for He used by Hunten et al. (1989) which is 5.1×10^{-5} photons atoms^{-1} s^{-1} is consistent with similar studies such as Broadfoot et al. (1976), Killen et al. (2022). Additionally, a recalculation of the g-factor, based on the equation presented in Yoneda et al. (2021) yielded results consistent with those in Killen et al. (2022). However, if one applies these g-factors and the parameters given in Table 1 of Broadfoot et al. (1976) and Hunten et al. (1989) one cannot reproduce the brightness values of 70 R but the obtained values are about an order of magnitude smaller which, surprisingly, also corresponds well with the values obtained from the PHEBUS instrument Quémerais et al. (2023). These inconsistencies, however, raise questions about the accuracy of the He radiances shown in Broadfoot et al. (1976), Hunten et al. (1989). In the study of Quémerais et al. (2023), discussions evolved around the possibilities of potential causes or calibration errors of the PHEBUS instrument, given the significant discrepancies in measurement results compared to Mariner 10. As Figure 5 shows, the results conducted within this study align very well with the results from PHEBUS, which means that there might be an error within the Mariner 10 data.

It is worth noting that Jian et al. (2010) demonstrated the existence of He^+ generated ICWs in the solar wind. However, waves within the solar wind frame exhibit significantly higher velocities than the spacecraft, causing a frequency shift toward higher frequencies. This means that with our used methodology the He^+-ICWs within the solar wind are not detected and so it can be said that all observed ICWs are all generated by planetary ions. Additionally, a study from Yoneda et al. (2021) showed that the density of He may change with the orbital phase. Such a dependence was not observed in this study.

5. Conclusions

Here we present the first detection of neutral He in Mercury's extended exosphere at distances ≥1.5 Mercury radii derived from in situ magnetic field measurements. We measure exospheric He number densities from $n = 50$ cm^{-3} to $n = 0.3$ cm^{-3} between 1 R_M to 6 R_M, which we show to be consistent with a day-side thermal Helium population with $n_{surf} = 1{,}100$ cm^{-3} at $T_{surf} = 615$ K. By comparison with an independently derived Helium model, the density measurements were shown to be consistent with a dayside thermal Helium population with $n_{surf} = 1{,}100$ cm^{-3} at $T_{surf} = 615$ K. The measurement points indicative of more energetic Helium were fit using a Chamberlain profile with $n_{surf} = 150$ cm^{-3} and $T_{rel} = 2700$ K, which can be interpreted as Helium release through sporadic meteorite events. The number density profile of He, determined in this study lies within the ranges of the measurements conducted recently by BepiColombo's PHEBUS instrument Quémerais et al. (2023). The estimated He surface density lies between that of Hunten et al. (1989) and Quémerais et al. (2023), nevertheless more detailed studies about the energetic He population and its possible origin in sporadic surface erosion through mid-sized meteoroid impact are necessary (see Hener et al. (2024)). This can be accomplished with the arrival of the two spacecraft mission BepiColombo at Mercury in 2026. New observations will then provide opportunities to further refine the particle analysis method applied in this study. As the magnetic field data from the Mercury Magnetometer (MERMAG) (Baumjohann et al., 2020) can be used to identify ICWs and estimate ion densities from these waves, as described in the methods section. This data will allow a direct comparison of ion densities derived from ICW analysis with measurements from the ion sensors on BepiColombo (SERENA-PICAM and MPPE-MSA), which will detect ions in Mercury's environment. Such a comparative analysis will enable a statistical determination of the energy transfer efficiency parameter and, for the first time, measure it in situ. Additionally, the neutral gas density estimated using our method can be cross-validated with data from SERENA (Orsini et al., 2010, 2021) and MPPE (Saito et al., 2021). These in situ measurements will help assess whether the assumed 100 gyrations for ICW development is realistic or if this parameter needs to be revised. The combined data sets from MERMAG, MPPE and SERENA will provide a robust foundation for improving our understanding of Mercury's plasma and exospheric environment.

Data Availability Statement

The magnetic field (MAG) data from the MESSENGER spacecraft are available to the public through the NASA Planetary Data System (PDS) and can be accessed on their website (Korth, 2021): https://pds-ppi.igpp.ucla.edu/search/view/?f=yes&id=pds://PPI/mess-mag-calibrated/data/mso. The solar wind density and velocity data were sourced from the Automated Multi-Dataset Analysis (Génot, 2021) database. These open-access data can be downloaded from their website via the Workspace Explorer under Solar Wind Propagation Models/Mercury/Tao

Model/SW/Input OMNI: http://amda.cdpp.eu/. Information on Mercury's orbital motion was obtained from the Navigation and Ancillary Information Facility (Acton, 1996) and is publicly accessible on the NASA Jet Propulsion Laboratory (JPL) webpage: https://naif.jpl.nasa.gov/pub/naif/pds/data/mess-e_v_h-spice-6-v1.0/messsp_1000/data/spk/. The solar spectral irradiance at Mercury's orbit, used to determine solar activity during the event observations, was acquired from the Flare Irradiance Spectral Model for Mercury (FISM-P), provided by the LASP Interactive Solar Irradiance Datacenter (Chamberlin et al., 2008), accessible at: https://lasp.colorado.edu/lisird/data/fism_p_ssi_mercury/.

Acknowledgments

FW would like to thank Magda Delva for their advises and interesting conversations about ICWs. CSW was funded by the Austrian Science Fund (FWF) 10.55776/P35954. We thank Dr. Rozenn Robidel and another anonymous referee for a thorough read of our manuscript and useful comments during the review process. Open access funding provided by Osterreichische Akademie der Wissenschaften/KEMö.

References

Acton, C. H. (1996). Ancillary data services of NASA's navigation and ancillary information facility. *Planetary and Space Science*, *44*(1), 65–70. https://doi.org/10.1016/0032-0633(95)00107-7

Anderson, B. J., Acuña, M. H., Lohr, D. A., Scheifele, J., Raval, A., Korth, H., & Slavin, J. A. (2007). The magnetometer instrument on Messenger. *Space Science Reviews*, *131*(1–4), 417–450. https://doi.org/10.1007/s11214-007-9246-7

Andrews, G. B., Zurbuchen, T. H., Mauk, B. H., Malcom, H., Fisk, L. A., Gloeckler, G., et al. (2007). The energetic particle and plasma spectrometer instrument on the Messenger spacecraft. *The Messenger Mission to Mercury*, 523–556. https://doi.org/10.1007/978-0-387-77214-1_15

Baumjohann, W., Matsuoka, A., Narita, Y., Magnes, W., Heyner, D., Glassmeier, K.-H., et al. (2020). The BepiColombo–mio magnetometer en route to Mercury. *Space Science Reviews*, *216*(8), 125. https://doi.org/10.1007/s11214-020-00754-y

Berezhnoy, A. A., & Klumov, B. A. (2008). Impacts as sources of the exosphere on Mercury. *Icarus*, *195*(2), 511–522. https://doi.org/10.1016/j.icarus.2008.01.005

Brain, D. A., Bagenal, F., Acuña, M. H., Connerney, J. E., Crider, D. H., Mazelle, C., et al. (2002). Observations of low-frequency electromagnetic plasma waves upstream from the martian shock. *Journal of Geophysical Research*, *107*(A6). https://doi.org/10.1029/2000ja000416

Brinca, A. L. (1991). Cometary linear instabilities: From profusion to perspective. In A. D. Johnstone (Ed.), *Cometary plasma processes*, *Geophys. Monograph Series* (Vol. 61, pp. 211–221). AGU. https://doi.org/10.1029/GM061p0211

Broadfoot, A. L., Kumar, S., Belton, M. J., & McElroy, M. B. (1974). Mercury's atmosphere from mariner 10: Preliminary results. *Science*, *185*(4146), 166–169. https://doi.org/10.1126/science.185.4146.166

Broadfoot, A. L., Shemansky, D. E., & Kumar, S. (1976). Mariner 10: Mercury atmosphere. *Geophysical Research Letters*, *3*(10), 577–580. https://doi.org/10.1029/gl003i010p00577

Chamberlain, J., & Hunten, D. (1987). *Theory of planetary atmospheres*. Academic Press. Retrieved from https://books.google.at/books?id=vPRQAAAAMAAJ

Chamberlin, P. C., Woods, T. N., & Eparvier, F. G. (2008). Flare irradiance spectral model (FISM): Flare component algorithms and results. *Space Weather*, *6*(5), S05001. https://doi.org/10.1029/2007sw000372

Cintala, M. J. (1992). Impact-induced thermal effects in the lunar and Mercurian regoliths. *Journal of Geophysical Research*, *97*(E1), 947–973. https://doi.org/10.1029/91je02207

Cowee, M. M., Gary, S. P., & Wei, H. Y. (2012). Pickup ions and ion cyclotron wave amplitudes upstream of Mars: First results from the 1D Hybrid Simulation. *Geophysical Research Letters*, *39*(8), L08104. https://doi.org/10.1029/2012gl051313

Cowee, M. M., Winske, D., Russell, C. T., & Strangeway, R. J. (2007). 1D hybrid simulations of planetary ion-pickup: Energy partition. *Geophysical Research Letters*, *34*(2), L02113. https://doi.org/10.1029/2006gl028285

Delva, M., Bertucci, C., Volwerk, M., Lundin, R., Mazelle, C., & Romanelli, N. (2015). Upstream proton cyclotron waves at Venus near solar maximum. *Journal of Geophysical Research: Space Physics*, *120*(1), 344–354. https://doi.org/10.1002/2014ja020318

Delva, M., Mazelle, C., Bertucci, C., Volwerk, M., Vörös, Z., & Zhang, T. L. (2011). Proton cyclotron wave generation mechanisms upstream of Venus. *Journal of Geophysical Research (Space Physics)*, *116*(A2), A02318. https://doi.org/10.1029/2010JA015826

Delva, M., Volwerk, M., Mazelle, C., Chaufray, J. Y., Bertaux, J. L., Zhang, T. L., & Vörös, Z. (2009). Hydrogen in the extended Venus exosphere. *Geophysical Research Letters*, *36*(1), L01203. https://doi.org/10.1029/2008gl036164

Delva, M., Zhang, T. L., Volwerk, M., Vörös, Z., & Pope, S. A. (2008). Proton cyclotron waves in the solar wind at Venus. *Journal of Geophysical Research (Planets)*, *113*(A6), E00B06. https://doi.org/10.1029/2008JE003148

Eichhorn, G. (1978). Heating and vaporization during hypervelocity particle impact. *Elsevier*, *26*(5), 463–467. https://doi.org/10.1016/0032-0633(78)90067-3

Gary, S. P. (1991). Electromagnetic ion/ion instabilities and their consequences in space plasmas: A review. *Space Science Reviews*, *56*(3–4). https://doi.org/10.1007/bf00196632

Gary, S. P., Fuselier, S. A., & Anderson, B. J. (1993). Ion anisotropy instabilities in the magnetosheath. *Journal of Geophysical Research*, *98*(A2), 1481–1488. https://doi.org/10.1029/92JA01844

Génot, V. (2021). Automated multi-dataset analysis (AMDA): An on-line database and analysis tool for heliospheric and planetary plasma data [Dataset]. *NASA*. https://doi.org/10.1016/j.pss.2021.105214

Goldstein, B. E., Suess, S. T., & Walker, R. J. (1981). Mercury: Magnetospheric processes and the atmospheric supply and loss rates. *Journal of Geophysical Research*, *86*(A7), 5485–5499. https://doi.org/10.1029/ja086ia07p05485

Grava, C., Retherford, K., Hurley, D., Feldman, P., Gladstone, G., Greathouse, T., et al. (2016). Lunar exospheric helium observations of LRO/LAMP coordinated with Artemis. *Icarus*, *273*, 36–44. https://doi.org/10.1016/j.icarus.2015.10.033

Gruntman, M. (1997). Energetic neutral atom imaging of Space Plasmas. *Review of Scientific Instruments*, *68*(10), 3617–3656. https://doi.org/10.1063/1.1148389

Hartle, R. E., Curtis, S. A., & Thomas, G. E. (1975). Mercury's Helium exosphere. *Journal of Geophysical Research*, *80*(25), 3689–3692. https://doi.org/10.1029/JA080i025p03689

Hasegawa, A. (1969). Drift mirror instability in the magnetosphere. *Physics of Fluids*, *12*, 2642–2650. https://doi.org/10.1063/1.1692407

Hener, J., Wurz, P., Weichbold, F., Lammer, H., Schmid, D., & Vorburger, A. (2024). The Hermean Helium Exosphere—Continuous and sporadic Helium release processes. https://doi.org/10.1029/2024JE008696

Hodges, R. R., & Johnson, F. S. (1968). Lateral transport in planetary exospheres. *Journal of Geophysical Research*, *73*(23), 7307–7317. https://doi.org/10.1029/ja073i023p07307

Huddleston, D. E. (1990). *The interaction between a comet and the solar wind*. UCL (University College London).

Huddleston, D. E., & Johnstone, A. D. (1992). Relationship between wave energy and free energy from pickup ions in the comet Halley Environment. *Journal of Geophysical Research*, *97*(A8), 12217–12230. https://doi.org/10.1029/92ja00726

Huddleston, D. E., Johnstone, A. D., Coates, A. J., & Neubauer, F. M. (1991). Quasi-linear pitch angle and energy diffusion of pickup ions near comet Halley. *Journal of Geophysical Research*, *96*(A12), 21329–21341. https://doi.org/10.1029/91ja02169

Huddleston, D. E., Strangeway, R. J., Warnecke, J., Russell, C. T., & Kivelson, M. G. (1998). Ion cyclotron waves in the IO torus: Wave dispersion, free energy analysis, and so2+ source rate estimates. *Journal of Geophysical Research*, *103*(E9), 19887–19899. https://doi.org/10.1029/97je03557

Huebner, W., & Mukherjee, J. (2015). Photoionization and photodissociation rates in solar and blackbody radiation fields. *Planetary and Space Science*, *106*, 11–45. https://doi.org/10.1016/j.pss.2014.11.022

Hunten, D. M., Morgan, T. H., & Shemansky, D. E. (1989). The Mercury atmosphere. *Mercury*, 562–612. https://doi.org/10.2307/j.ctv1v090nx.21

Hurley, D. M., Cook, J. C., Benna, M., Halekas, J. S., Feldman, P. D., Retherford, K. D., et al. (2016). Understanding temporal and spatial variability of the lunar helium atmosphere using simultaneous observations from LRO, Ladee, and Artemis. *Icarus*, *273*, 45–52. https://doi.org/10.1016/j.icarus.2015.09.011

Jian, L. K., Russell, C. T., Luhmann, J. G., Anderson, B. J., Boardsen, S. A., Strangeway, R. J., et al. (2010). Observations of ion cyclotron waves in the solar wind near 0.3 AU. *Journal of Geophysical Research*, *115*(A12), A12115. https://doi.org/10.1029/2010ja015737

Kallio, E., & Janhunen, P. (2003). Solar wind and magnetospheric ion impact on Mercury's surface. *Geophysical Research Letters*, *30*(17), 1877. https://doi.org/10.1029/2003GL017842

Killen, R., Cremonese, G., Lammer, H., Orsini, S., Potter, A. E., Sprague, A. L., et al. (2007). Processes that promote and deplete the exosphere of Mercury. *Space Science Reviews*, *132*(2–4), 433–509. https://doi.org/10.1007/s11214-007-9232-0

Killen, R., Potter, A. E., Reiff, P., Sarantos, M., Jackson, B. V., Hick, P., & Giles, B. (2001). Evidence for space weather at Mercury. *Journal of Geophysical Research*, *106*(E9), 20509–20525. https://doi.org/10.1029/2000je001401

Killen, R., Vervack, R. J., Jr., & Burger, M. (2022). Updated photon scattering coefficients g_values for Mercury's exospheric species. *The Astrophysical Journal - Supplement Series*, *263*(2), 37. https://doi.org/10.3847/1538-4365/ac9eab

Korth, H. (2021). PDS: Collection information [Dataset]. *NASA*. Retrieved from https://pds.nasa.gov/doi:10.17189/1522385

Leblanc, F., & Chaufray, J.-Y. (2011). Mercury and Moon He exospheres: Analysis and modeling. *Icarus*, *216*(2), 551–559. https://doi.org/10.1016/j.icarus.2011.09.028

Mangano, V., Milillo, A., Mura, A., Orsini, S., De Angelis, E., Di Lellis, A., & Wurz, P. (2007). The contribution of impulsive meteoritic impact vapourization to the Hermean exosphere. *Planetary and Space Science*, *55*(11), 1541–1556. https://doi.org/10.1016/j.pss.2006.10.008

Marchi, S., Morbidelli, A., & Cremonese, G. (2005). Flux of meteoroid impacts on Mercury. *Astronomy & Astrophysics*, *431*(3), 1123–1127. https://doi.org/10.1051/0004-6361:20041800

Mazelle, C., & Neubauer, F. M. (1993). Discrete wave packets at the proton cyclotron frequency at Comet P/Halley. *Geophysical Research Letters*, *20*(2), 153–156. https://doi.org/10.1029/92gl02613

Means, J. D. (1972). Use of the three-dimensional covariance matrix in analyzing the polarization properties of Plane Waves. *Journal of Geophysical Research*, *77*(28), 5551–5559. https://doi.org/10.1029/ja077i028p05551

Morgan, T., Zook, H., & Potter, A. (1988). Impact-driven supply of sodium and potassium to the atmosphere of Mercury. *Icarus*, *75*(1), 156–170. https://doi.org/10.1016/0019-1035(88)90134-0

Narita, Y. (2017). Review article: Wave analysis methods for space plasma experiment. *Nonlinear Processes in Geophysics*, *24*(2), 203–214. https://doi.org/10.5194/npg-24-203-2017

Orsini, S., Livi, S., Torkar, K., Barabash, S., Milillo, A., Wurz, P., et al. (2010). Serena: A suite of four instruments (Elena, Strofio, PICAM and MIPA) on board BepiColombo-MPO for particle detection in the Hermean environment. *Planetary and Space Science*, *58*(1–2), 166–181. https://doi.org/10.1016/j.pss.2008.09.012

Orsini, S., Livi, S. A., Lichtenegger, H., Barabash, S., Milillo, A., De Angelis, E., et al. (2021). Serena: Particle instrument suite for determining the Sun-Mercury interaction from BepiColombo. *Space Science Reviews*, *217*(1), 11. https://doi.org/10.1007/s11214-020-00787-3

Philpott, L. C., Johnson, C. L., Anderson, B. J., & Winslow, R. M. (2020). The shape of Mercury's magnetopause: The picture from Messenger magnetometer observations and future prospects for BepiColombo. *Journal of Geophysical Research: Space Physics*, *125*(5), e2019JA027544. https://doi.org/10.1029/2019ja027544

Quémerais, E., Koutroumpa, D., Lallement, R., Sandel, B. R., Robidel, R., Chaufray, J., et al. (2023). Observation of helium in Mercury's exosphere by phebus on bepi-colombo. *Journal of Geophysical Research: Planets*, *128*(6), e2023JE007743. https://doi.org/10.1029/2023je007743

Raines, J. M., Gershman, D. J., Zurbuchen, T. H., Sarantos, M., Slavin, J. A., Gilbert, J. A., et al. (2013). Distribution and compositional variations of plasma ions in Mercury's space environment: The first three Mercury Years of messenger observations. *Journal of Geophysical Research: Space Physics*, *118*(4), 1604–1619. https://doi.org/10.1029/2012ja018073

Rönnmark, K. (1982). *WHAMP-Waves in homogeneous anisotropic multicomponent plasmas*. Rep (Vol. 179). Kiruna Geophys Institute.

Russell, C. (2005). Interaction of the galilean moons with their plasma environments. *Planetary and Space Science*, *53*(5), 473–485. https://doi.org/10.1016/j.pss.2004.05.003

Russell, C., Kivelson, M., Khurana, K., & Huddleston, D. (1998). Magnetic fluctuations close to io: Ion cyclotron and mirror mode wave properties. *Planetary and Space Science*, *47*(1–2), 143–150. https://doi.org/10.1016/s0032-0633(98)00090-7

Russell, C. T., Luhmann, J. G., Schwingenschuh, K., Riedler, W., & Yeroshenko, Y. (1990). Upstream waves at Mars: Phobos observations. *Geophysical Research Letters*, *17*(6), 897–900. https://doi.org/10.1029/gl017i006p00897

Saito, Y., Delcourt, D., Hirahara, M., Barabash, S., André, N., Takashima, T., et al. (2021). Pre-flight calibration and near-earth commissioning results of the Mercury plasma particle experiment (MPPE) onboard MMO (Mio). *Space Science Reviews*, *217*(5), 70. https://doi.org/10.1007/s11214-021-00839-2

Samson, J. C., & Olson, J. V. (1980). Some comments on the descriptions of the polarization states of waves. *Geophysical Journal International*, *61*(1), 115–129. https://doi.org/10.1111/j.1365-246x.1980.tb04308.x

Schmid, D., Lammer, H., Plaschke, F., Vorburger, A., Erkaev, N. V., Wurz, P., et al. (2022). Magnetic evidence for an extended hydrogen exosphere at Mercury. *Journal of Geophysical Research: Planets*, *127*(11), e2022JE007462. https://doi.org/10.1029/2022JE007462

Schmid, D., Narita, Y., Plaschke, F., Volwerk, M., Nakamura, R., & Baumjohann, W. (2021). Pick-up ion cyclotron waves around Mercury. *Geophysical Research Letters*, *48*(9), e2021GL092606. https://doi.org/10.1029/2021gl092606

Solomon, S. C., McNutt, R. L., Gold, R. E., & Domingue, D. L. (2007). Messenger mission overview. *Space Science Reviews*, *131*(1–4), 3–39. https://doi.org/10.1007/s11214-007-9247-6

Southwood, D. J., & Kivelson, M. G. (1993). Mirror instability: 1. Physical mechanism of linear instability. *Journal of Geophysical Research*, *98*(A6), 9181–9187. https://doi.org/10.1029/92JA02837

Sun, W., Dewey, R. M., Aizawa, S., Huang, J., Slavin, J. A., Fu, S., et al. (2021). Review of Mercury's dynamic magnetosphere: Post-MESSENGER Era and comparative magnetospheres. *Science China Earth Sciences*, *65*(1), 25–74. https://doi.org/10.1007/s11430-021-9828-0

Tao, C., Kataoka, R., Fukunishi, H., Takahashi, Y., & Yokoyama, T. (2005). Magnetic field variations in the Jovian magnetotail induced by solar wind dynamic pressure enhancements. *Journal of Geophysical Research*, *110*(A11), A11208. https://doi.org/10.1029/2004ja010959

Thatcher, L., & Müller, H.-R. (2011). Statistical investigation of hourly OMNI solar wind data. *Journal of Geophysical Research*, *116*(A12), A12107. https://doi.org/10.1029/2011ja017027

Volwerk, M., Khurana, K. K., Roux, J. l., Zank, G. P., Coates, A. J., & Florinski, V. (2010). Ion pick-up near the Icy Galilean satellites. *AIP Conference Proceedings*, 263–269. https://doi.org/10.1063/1.3529982

Volwerk, M., Kivelson, M. G., & Khurana, K. K. (2001). Wave activity in Europa's wake: Implications for ion pickup. *Journal of Geophysical Research*, *106*(A11), 26033–26048. https://doi.org/10.1029/2000ja000347

Welch, P. (1967). The use of fast fourier transform for the estimation of power spectra: A method based on time averaging over short, modified periodograms. *IEEE Transactions on Audio and Electroacoustics*, *15*(2), 70–73. https://doi.org/10.1109/tau.1967.1161901

Winslow, R. M., Johnson, C. L., Anderson, B. J., Korth, H., Slavin, J. A., Purucker, M. E., & Solomon, S. C. (2012). Observations of Mercury's northern cusp region with Messenger's magnetometer. *Geophysical Research Letters*, *39*(8), L08112. https://doi.org/10.1029/2012gl051472

Wurz, P., Fatemi, S., Galli, A., Halekas, J., Harada, Y., Jäggi, N., et al. (2022). Particles and photons as drivers for particle release from the surfaces of the Moon and Mercury. *Space Science Reviews*, *218*(3), 10. https://doi.org/10.1007/s11214-022-00875-6

Wurz, P., Gamborino, D., Vorburger, A., & Raines, J. M. (2019). Heavy ion composition of Mercury's magnetosphere. *Journal of Geophysical Research: Space Physics*, *124*(4), 2603–2612. https://doi.org/10.1029/2018ja026319

Wurz, P., & Lammer, H. (2003). Monte-Carlo simulation of Mercury's exosphere. *Icarus*, *164*(1), 1–13. https://doi.org/10.1016/s0019-1035(03)00123-4

Wurz, P., Whitby, J., Rohner, U., Martín-Fernández, J., Lammer, H., & Kolb, C. (2010). Self-consistent modelling of Mercury's exosphere by sputtering, micro-meteorite impact and photon-stimulated desorption. *Planetary and Space Science*, *58*(12), 1599–1616. https://doi.org/10.1016/j.pss.2010.08.003

Yoneda, M., Dima, G., & Berdyugina, S. V. (2021). Mercury's exospheric he i 58.4 nm emission: Dependence on the Orbital Phase. *Astronomy and Astrophysics*, *654*, L7. https://doi.org/10.1051/0004-6361/202142155